Design and test of a dual-axis layered rotary tillage stubble exterminator in saline-alkali land based on discrete elements

Zhuang Zhao[1], Dongwei Wang[2,3], Shuqi Shang[2], Peng Guo[1], Zenghui Gao[4], Chao Xia[4], Haipeng Yan[3], Jialin Hou[1*]

(1. *College of Mechanical and Electronic Engineering, Shandong Agricultural University, Tai'an 271018, Shandong, China*;
2. *College of Mechanical and Electrical Engineering, Qingdao Agricultural University, Qingdao 266109, Shandong, China*;
3. *Yellow River Delta Intelligent Agricultural Machinery Equipment Industry Research Institute Document, Dongying 257300, Shandong, China*;
4. *College of Mechanical and Electronic Engineering, Xinjiang Agricultural University, Urumqi 830052, China*)

Abstract: Considering the problems of low soil crushing rate and poor straw mulching performance of the traditional rotary tiller on saline-alkali soils, a two-axis layered rotary stubble cutter for saline-alkali soils with front-axis positive rotation of the front axle and rear-axis counter-rotation of the rear axle was developed, focusing on the kinetic properties of the straw and soil under positive and counter-rotation. In addition, the most important structural parameters and the arrangement of the front-axis stubble cutting knife and the rear-axis return knife were analyzed and determined. Hertz-Mindlin with bonding was used to create a discrete element model of the agglomerate of implement, straw and soil. The forward speed, horizontal distance and vertical distance were used as test factors, and the straw return rate and soil fragmentation rate were used as test indexes to analyze the straw-soil transport law under different operating parameters from a microscopic point of view, and then Design-Expert was used to conduct the test 1.07 km/h, horizontal distance of 569.55 mm, vertical distance of 176.59 mm. To validate the performance of the two-axis, layered rotary tiller, a field trial was conducted and the results show that the straw return ratio was (91.59±0.41)%, soil fragmentation ratio was (91.90±0.29)% and tillage depth stability was (91.52±0.46)%, which met the requirements for peanut seedbed preparation on saline-alkali land.

Keywords: saline-alkali land, straw return, soil fragmentation, dual-axis layering, discrete element simulation, field trial
DOI: 10.25165/j.ijabe.20241705.8950

Citation: Zhao Z, Wang D W, Shang S Q, Guo P, Gao Z H, Xia C, et al. Design and test of a dual-axis layered rotary tillage stubble exterminator in saline-alkali land based on discrete elements. Int J Agric & Biol Eng, 2024; 17(5): 163–175.

1 Introduction

Seedbed preparation is an important production aspect of peanut cultivation[1], and high-quality seedbeds can promote crop growth and increase crop yield[2]. The Yellow River Delta, with its low topography and poor drainage, has resulted in serious soil salinization in the region, which is prone to sloughing, making it difficult to prepare high-quality seed beds suitable for the growth of peanuts in saline-alkali lands, and seriously affecting peanut yields. At present, the preparation of peanut seedbed in the Yellow River Delta region is dominated by rotary tiller, but there are problems such as low straw return rate and soil fragmentation rate during operation, which cannot meet the requirements of large-scale peanut planting in the Yellow River Delta region, so the study of peanut high-quality seed bed preparation in saline-alkali lands has an important application value[3,4].

The discrete element method is a numerical method suitable for analyzing and solving the dynamics of complex discrete systems, which can effectively solve the nonlinear problem of the interaction between the soil and the tillage components[5-8], and obtain the information of the data that cannot be measured by field experiments from a fine viewpoint, so as to realize the prediction of the performance of the tillage system and the optimization of the parameters[9-12]. Scholars at home and abroad have mainly focused on the assessment of indicators and soil displacement after tillage, and the discrete element model for rotary tillage operation in saline and alkaline land is less involved, which cannot deduce the actual rule of change of soil tillage layer in saline-alkali lands.

Li et al.[13] designed an oilseed rape rotary-cutting micromonocline seed bed preparation device, which can achieve the functions of soil crushing, furrowing, ridging, and sowing seeds on the ridge, and combined with EDEM simulation tests to determine the optimal working parameters. Chen et al.[14] established a soil-straw composite model for undisturbed soil under straw coverage conditions, the combination of three types of ST and RT was studied using coupled DEM-MFBD simulations, the field test results showed that coupled simulation technology can predict the operating quality and deformation stress of the machine. Zhou et al.[15] conducted via three types of tillage tools in rice stubble fields, analyzed the mulching rate of straw under different soil layers, and the results show that a subsoiling+straw rotary burying and returning machine was the most desirable tillage tool. Jia et al.[16]

Received date: 2024-03-24 **Accepted date:** 2024-07-30
Biographies: Zhuang Zhao, PhD, research interest: agricultural machinery and equipment, Email: 20192204158@stu.qau.edu.cn; **Dongwei Wang**, PhD, research interest: agricultural machinery and equipment, Email: w88030661@163.com; **Shuqi Shang**, Professor, research interest: agricultural machinery and equipment, Email: sqshang@qau.edu.com; **Peng Guo**, PhD, research interest: agricultural mechanization, Email: 1669753064@qq.com; **Zenghui Gao**, PhD, research interest: agricultural mechanization, Email: GaoQAU@163.com; **Chao Xia**, PhD, research interest: agricultural mechanization, Email: 20192204156@stu.qau.edu.cn; **Haipeng Yan**, MS, research interest: agricultural mechanization, Email: 519042925@qq.com.
***Corresponding author: Jialin Hou**, PhD, Professor, research interest: design and theory of agricultural equipment. College of Mechanical and Electronic Engineering, Shandong Agricultural University, Tai'an 271018, Shandong, China. Tel: +86-13605388153, Email: jlhou@sdau.edu.cn.

developed a combined stalk–stubble breaking and mulching machine with two frames fixed together and can be used to break the maize stalk and stubble and bury, which meets the agro-technical requirements in the dry farming area of northern China. Torotwa et al.[17] fabricated a biomimetic disc mimicking the mole-rat's claw and evaluated in comparison with traditional discs, combining theoretical analysis and soil bin tests, the optimum working and structural parameters were determined. Barbosa[18] designed a plowing tool for sugarcane planting, analyzed the fragmentation characteristics and energy requirements of soil tillage tools in the formation of seedbeds, The new tool concept showed potential to decrease the power demand by 28.5% at the same time it increases the fractal fragmentation by 10% in comparison to the conventional tool. Saunders et al.[19] systematically analyzed the influence of parameters such as plough forward speed, operating depth and entry angle on soil movement, and combined with field experiments, showed that EDEM can effectively evaluate soil movement mechanisms. Azimi-Nejadian et al.[20] analyzed the relationship between the structural parameters of the plough body curved surfaces and the operating parameters on the weed burying performance and soil movement effects, using tracers for weed and soil identification, and the tests showed that EDEM can be used as a tool to optimize the operational performance of soil-touching components. Shaikh et al.[21] analyzed the soil movement laws at 7.5%, 21.5%, and 38.0% soil moisture content using EDEM system and combined with soil trench test, the minimum error between the simulation test results and the soil trench test results was 10.09%, which shows the accuracy of discrete element method to analyze the soil movement laws.

To solve the poor straw mulching performance, low soil crushing rate and poor straw mulching performance for the peanut seedbed preparation on saline-alkali land, based on the physical properties of saline soil-straw and the requirements of stubble crushing, this paper proposes a dual-axis stratified rotary stubble cutter with front-axis positive rotation and rear-axis counter-rotation, and the discrete element model of soil-straw-equipment was constructed by using EDEM. The systematic investigation of the knife axis vertical spacing, horizontal spacing, forward speed test factors on the performance of saline soil crushing - stubble, combined with field tests to determine the best working parameters and structural parameters of the machine, for the preparation of high-quality seedbed of peanuts in saline-alkali lands to lay a solid foundation.

2 Experiment materials and methods

2.1 Machine structure and working principle

At present, the dual-axis rotary operation mode is mainly divided into front-axis positive rotation, rear-axis counter-rotation, dual-axis positive rotation, front-axis counter-rotation, rear-axis positive rotation and other forms. This paper combines the physical characteristics of alkaline soil and the agronomic requirements of peanut planting, innovative design of a front-axis positive rotation, rear-axis counter-rotation stratified rotary plow stubble machine, the structure of the whole machine as shown in Figure 1, mainly by the frame, three-point suspension device, positive rotation stubble device, counter-rotation crushing device, crushing drag plate and transmission system and other institutions. The working principle is shown in Figure 2, as the machine advances, the positive rotation stubble device throws the straw-soil agglomerate backward along the tangent line of the rotary cutter for preliminary crushing, and the counter-rotary crushing device crushes the soil-straw initially crushed by the stubble cutter, as well as the soil-straw that is not crushed for the second time to be crushed and buried, so as to form a high-quality seed bed with a false upper and a false lower, and the main technical parameters are listed in Table 1.

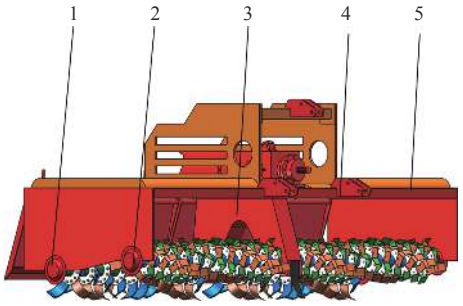

1. Counter-rotation crushing device, 2. Positive rotation stubble device, 3. Transmission system, 4. Three-point suspension device, 5. Frame

Figure 1 Double-shaft stratified rotary ploughing and stubble removal machine structure

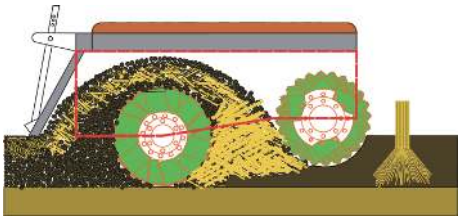

Figure 2 Working principle of double-shaft stratified rotary ploughing and stubble removal machine

Table 1 Parameters of rotary tiller

Parameters	Value
Size of the whole machine/mm×mm×mm	1750×2580×1350
Forward velocity/km·h^{-1}	1-5
Maximum tillage depth of stubble knife/mm	100
Maximum tillage depth of return knife/mm	150
Rotation speed of stubble knife/r·min^{-1}	430-520
Rotation speed of returnable knife/r·min^{-1}	280-340
Working width/mm	2300
Motive power/kW	≥100

2.2 Analysis of stubble knife-soil-straw dynamics

To further enhance high-quality soil crushing and straw mulching in saline-alkali lands, the kinetic analysis of the front-axis stubble knife was carried out, and the interactions between the stubble knife-soil thickness-throwing angle under different operating parameters were investigated, and a mathematical model of the stubble knife's movement trajectory and soil collision and throwing was established.

As shown in Figure 3, the stubble knife axis as the center of rotation, the forward direction as the X-axis, the vertical direction as the Y-axis, to establish the stubble knife operating coordinate system. When the stubble knife is working, the trajectory of the blade endpoint at point $B(X, Y)$ is obtained.

$$\begin{cases} X_x = v_m t - R\cos\omega t \\ Y_y = R\sin\omega t \end{cases} \quad (1)$$

where, X_x is the displacement component of stubble cutter along X-axis at point B, mm; Y_y is the displacement component of stubble cutter along Y-axis at point B, mm; v_m is the forward velocity of the implement, m/s; R is the turning radius of stubble knife, mm; ω is the angular velocity of stubble knife, rad/s; t is the stubble knife operation time, s.

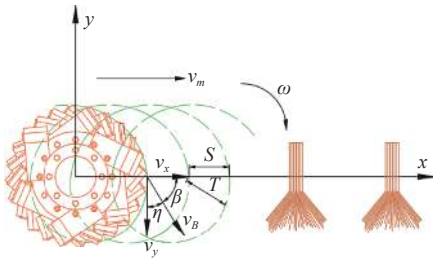

Note: v_m is the forward velocity of the implement, m/s; R is the turning radius of stubble knife, mm; ω is the angular velocity of stubble knife, rad/s; t is the stubble knife operation time, s; T is the soil-straw cutting thickness, mm; S is the stubble knife operating pitch, mm; β is the angle of absolute speed of stubble knife with X-axis, (°); η is the angle of absolute speed of stubble knife with Y-axis, (°); v_x is the velocity component of stubble cutter along X-axis, m/s; v_y is the velocity component of stubble cutter along Y-axis, m/s; v_B is the absolute speed of stubble knife, m/s.

Figure 3 Analysis of stubble cutter-straw-soil dynamics

In order to improve the efficiency of the stubble cutter in cutting and conveying the straw-soil, it is necessary to ensure that the trajectory of the stubble cutter is a cycloid.

$$\lambda = \frac{R\omega}{v_m} > 1 \tag{2}$$

where, λ is the ratio of rotary plowing speed.

To ensure the stubble knife can achieve continuous and orderly cutting of soil-straw during operation, combined with the geometric relationship in Figure 3, the stubble knife adjacent to the operating track and the untilled area needs to meet the following requirements:

$$T \approx S\sin\beta \tag{3}$$

$$S = \frac{2\pi v_m}{z\omega} \tag{4}$$

$$\beta = \arctan\frac{v_y}{v_x} \tag{5}$$

where, z is the number of stubble knives in the same section.

The soil-straw cutting thickness during stubble knife operation was obtained as:

$$T \approx \frac{2\pi R}{z\lambda}\sin\left(\arctan\frac{\lambda\cos\omega t}{1+\lambda\sin\omega t}\right) \tag{6}$$

Combined with Equation (6), the main factors affecting the stubble knife soil-straw cutting thickness are the forward speed v_m, the number of stubble knife installed in the same section z, the stubble knife angular velocity ω, the stubble knife turning radius R, which lays the foundation for the subsequent design of stubble knife structural parameters and operating parameters.

2.3 Straw cross-section dynamics analysis

In order to study the stubble knife-straw cutting kinetic analysis and reveal the mechanism of stubble knife crushing soil and straw burying, As shown in Figures 4-6, focused on straw kinetic analysis in B and D cutting position, and the yellow part represents the straw, and the black part represents the cutting-edge curve of the stubble knife cutting straw.

The maximum friction between the straw and the stubble knife is

$$f_{\max} = N\tan a_f \tag{7}$$

where, $f_{\max}$ is the maximum friction between straw and stubble knife, N; a_f is the angle of friction between straw and stubble knife, (°).

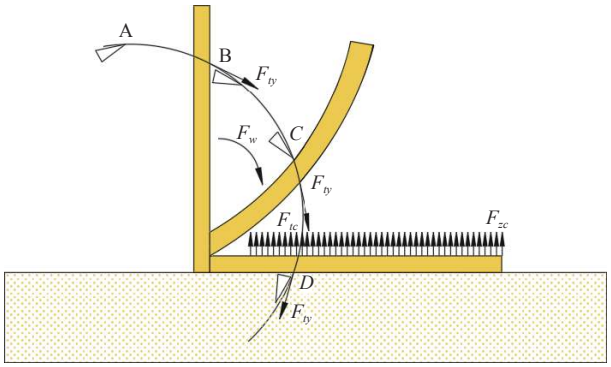

Figure 4 Schematic diagram of wheat straw crushing and mulching

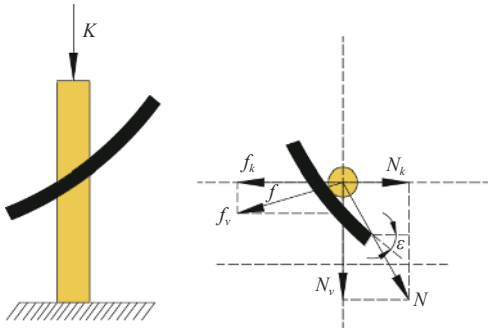

Figure 5 Analysis of straw dynamics at point B

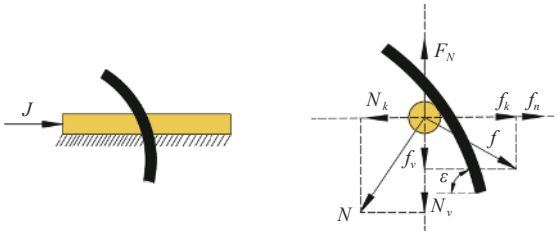

Note: N is the push force of the stubble knife on the straw, N; N_k is the horizontal component of the push force, N; N_v is the vertical component of the push force, N; f is the friction force of the stubble knife on the straw, N; f_k is the horizontal component of the friction force, N; f_v is the vertical component of the friction force, N; F_N is the support force of the ground on the straw, N; f_N is the friction force of the ground on the straw, N; ε is the angle of the sliding cut, (°); J and K are the squeezing forces of the knife disc on the straw, N.

Figure 6 Analysis of straw dynamics at point D

At cutting position B, the critical condition generated when the stubble knife slides to cut the straw is:

$$f_{\max} = f = N\tan\varepsilon \tag{8}$$

When the slip angle $\varepsilon > a_f$, stubble knife sliding cut wheat straw, straw along the direction of the knife edge occurs to produce the phenomenon of slippage, when the slip angle $\varepsilon < a_f$, stubble knife cut straw, wheat straw in the stubble knife blade under the action of the synchronized movement of the push pressure.

At cutting position D, the critical condition generated when the stubble knife slides to cut the straw is:

$$N\tan\varepsilon = N\tan a_f + \frac{f_N}{\cos\varepsilon} \tag{9}$$

Combined with reference[22,23], the friction angle between the wheat straw and the stubble knife blade ranges from 26° to 45°, and in order to improve the de-attachment ability of the stubble knife and the wheat straw, the sliding cut angle of the stubble knife's positive cutting edge is set to 45°.

2.4 Stubble knife side cutting edge curve design

The front axle stubble cutter side cutting edge curve design adopts Archimedean spiral, which can ensure that the sliding cutting angle and the radius of gyration increase synchronously during the cutting process, and at the same time, the Archimedean spiral can increase the depth of ploughing, reduce the working resistance as well as avoid the phenomenon of grass entanglement in the shank of the stubble knife, which can further improve the performance of the soil-straw throwing desorption, and the equation of the curve is as follows

$$\rho_1 = \sqrt{R^2+S^2-2S\sqrt{2Rh-h^2}} + \frac{\rho_n - \sqrt{R^2+S^2-2S\sqrt{2Rh-h^2}}}{\theta_n}\theta \tag{10}$$

where, ρ_1 is the pole diameter of the helix at any point, mm; θ is the polar angle at any point of the helix, rad; h is the depth of tillage of stubble knife, mm; ρ_n is the helix terminal pole diameter, mm; θ_n is the polar angle of the end point of the helix, rad.

The relationship between the polar angle θ_n and the slip tangent angle τ_n at the terminus of the Archimedean spiral at the terminus is

$$\theta_n = \left(\rho_n - \sqrt{R_1^2+S^2-2S\sqrt{2R_1h-h^2}}\right)\frac{\tan\tau_n}{\rho_n} \tag{11}$$

As shown in Figure 7, the complete process of cutting straw from point L_2 to L_1 by the side cutting edge of the stubble cutter was systematically investigated, at the same time, the dynamic relationship between the stubble knife and the straw is the same at L_1 and L_2 points. The straw agglomerate with mass m is taken for analysis, and the straw is subjected to the normal counterforce F_2 and tangential friction f_2 at the L_2 point, and the normal counterforce F_2 is decomposed into T_2 and M_2 along the trajectory of the stubble knife and the tangential direction of the side-cutting edge curve. In order to ensure that the stubble knife in the process of operation of the straw along the edge curve sliding until the complete detachment, it is necessary to ensure that T_2 is greater than f_2.

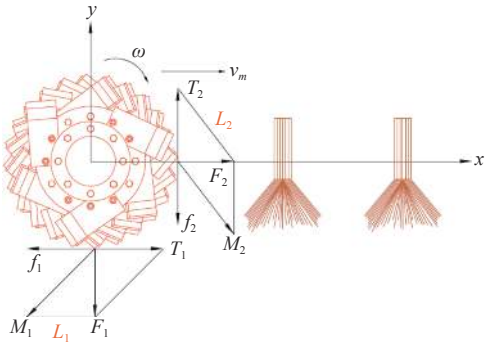

Note: F_2 is the normal reaction force of stubble knife edge curve at the L_2 point, N; f_2 is the tangential friction of stubble knife edge curve at the L_2 point, N; T_2 is the stubble knife edge curve tangential force at the L_2 point, N; M_2 is the tangential force on stubble knife trajectory at the L_2 point, N;

Figure 7 Schematic diagram of wheat straw cutting and throwing

$$\begin{cases} T_1 = M_1\tan\tau \\ f_1 = \mu F_1 \\ \mu = \tan\psi \end{cases} \tag{12}$$

where, φ is the angle of friction between straw and stubble knife, (°); μ is the friction factor between straw and stubble knife; τ is the dynamic slip-cut angle, (°).

In order to reduce the operating resistance of the stubble knife during operation, it is necessary to reduce the normal force on the edge curve and increase the tangential force on the edge curve, and the dynamic slip-cut angle needs to satisfy the following conditions:

$$\begin{cases} f_1 < T_1 \\ \mu < \tan\tau \\ \tan\varphi < \tan\tau \end{cases} \tag{13}$$

The dynamic slip-cut angle τ is related to the static slip-cut angle τ_1 in the following way:

$$\tau = \tau_1 - \Delta\tau \tag{14}$$

$$\Delta\tau = \arctan\frac{\sqrt{\rho_1^2-(R-\alpha)^2}}{\frac{\lambda}{R}\rho_1^2-(R-\alpha)} \tag{15}$$

where, τ_1 is the static slip-cut angle, (°); α is the distance of a point on the side cutting edge of the stubble knife from the bottom of the plough during operation, mm; $\Delta\tau$ is the errors caused by the advance of the machine during operation, (°).

Combined with Equation (15), $\Delta\tau$ of the stubble knife tends to decrease gradually during operation at a certain ratio of rotary plowing speed. Combined with reference[24], the friction factor μ of straw and steel is 0.68, and the friction angle is 34.57°, therefore, the dynamic slip-cut angle τ is greater than 34.57°. Combined with references[25,26], the dynamic slip-cut angle τ varies in the range of 43°-60°, and to ensure the operational performance, the slip-cut angle τ at the end of the curve of the side-cutting edge is taken to be 60°.

To improve the performance of stubble knife and straw slip cutting, ensure the stability of stubble knife plowing depth and stubble broken performance, stubble knife arrangement adopts spiral arrangement. Adjacent stubble knife installation spacing is 102 mm, the number of stubble knife installation in the same cross-section is 6, the installation angle is 60°. Each helical stubble knife adjacent to the installation angle is 5°, the number of stubble knife shaft blades is 120, of which the left side of the stubble knife shaft arrangement is shown in Figure 8. Combined with the basic physical properties of wheat, it is determined that the stubble knife operating depth h is 100 mm, and the radius of rotation R is 175 mm.

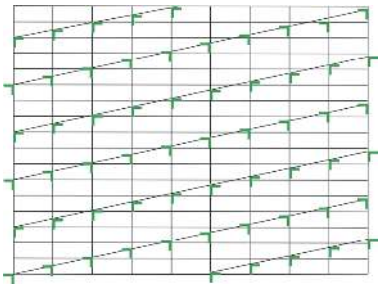

Figure 8 Arrangement of stubble knives

2.5 Analysis of returned knife-soil-straw dynamics

The rear axle is mainly used for soil-straw secondary crushing and mulching, and related research shows that the soil crushing, surface leveling, straw displacement and soil entry performance of counter-rotation operation are better than that of forward rotation operation[27]. Saline-alkali lands are easy to slough, hard and difficult to break, counter-rotation soil crushing operation can further improve the soil crushing and straw mulching performance. In this paper, an innovative design of a counter-rotating slip-cutting field return knife is adopted, with a double-helix arrangement, the

spacing of the cutter discs is 200 mm, the number of stubble knives installed in the same cross-section is 6, with an installation angle of 90°, and the angle of installation of neighboring cutter discs is 8°, and the arrangement of the left side of the knife axle of the field return knife is shown in Figure 9.

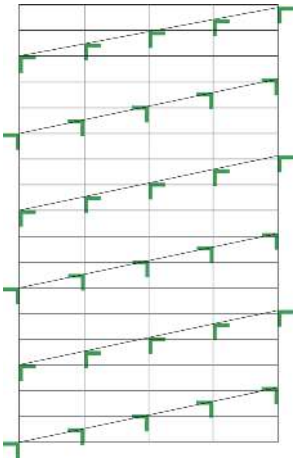

Figure 9 Arrangement of returned knives

As shown in Figure 10, the returning knife carries out soil crushing and straw burying operations from bottom to top, from near and far, assuming that the returning knife has an inelastic collision with the section G at soil A during the operation, and the soil after the collision is thrown under the combined action of reflection velocity and implication velocity, in order to realize the soil-straw aggregate ejection, the dynamic analysis of soil ejection is carried out, and the conditions for satisfying soil ejection are as follows:

$$v_t \cos\delta_1 + v_r \cos(\pi - \delta - \delta_1) \le 0 \tag{16}$$

where, δ_1 is the angle of incidence of soil, (°); δ is the angle of reflectance of soil, (°); v_t is the incidence velocity, m/s; v_r is the reflection velocity, m/s.

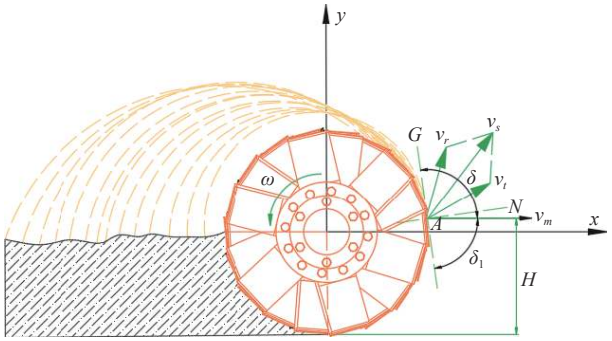

Figure 10 Analysis of returning knife-soil dynamics

The relationship between the reflection angle and the reflection velocity of soil particles is as follows:

$$\begin{cases} \delta = \arctan\left(\dfrac{k}{1-f}\tan\delta_1\right) \\ v_r = v_m(1-f)\dfrac{\cos\delta_1}{\cos\delta} \end{cases} \tag{17}$$

where, k is the coefficient of soil recovery, taken as 0.2 in this study; f is the soil-return knife friction coefficient, taken as 0.4 in this study.

Combined with the geometric relationship in Figure 10, the angle of incidence of soil is as follows:

$$\delta_1 = \tau_r - \arcsin\frac{H - R_1}{R_1} \tag{18}$$

where, τ_r is the positive cutting edge static sliding angle of field return cutter, (°) taken as 50° in this study; H is the maximum height of soil thrown by return cutter, mm; R_1 is the turning radius of return knife, mm.

The critical conditions for the backward throwing of soil by the returning knife are as follows:

$$k\frac{R_1 - H}{R_1} \le (1-f)\frac{\cos\delta_1\cos(\delta+\delta_1)}{\cos\delta} \tag{19}$$

The returning knife side cutting edge curve is designed by adopting the positive rotation index, which can prevent the phenomenon of hanging grass at the shank of the knife during the operation of the returning knife of the rear axle, and its calculation method is as follows:

$$\rho_1 = \rho_2\left(\frac{\sin\tau_0}{\sin(\tau_0 - K\theta_1)}\right)^{\frac{1}{k}} \tag{20}$$

where, ρ_1 is the returning knife side cutting edge curve; ρ_2 is the pole diameter at the beginning of the edge curve, mm; τ_0 is the static slip angle at start of edge curve, (°); K is the decreasing ratio of static slip angle of edge curve, mm; θ_1 is the polar angle of any point of the edge curve, (°).

Returning knife choose different edge curve starting point static slip angle and edge curve static slip angle decreasing ratio of operational performance is not the same. In this study, the design of the rear-axis field return knife operating depth h_1 is 150 mm, the radius of gyration R_1 is 250 mm, and the starting point of the cutting edge curve is 130 mm, in order to avoid the phenomenon of grass entanglement in the side-cutting edge of the rear-axis field return knife, it is necessary to ensure that the shank of the field return knife edge sliding angle of the blade is larger than the side-cutting edge curve sliding angle of the blade, and combined with the references[28,29], the static sliding angle of the blade is taken in the range of 35°-55°, the edge curve in this study, the static slip angle is taken as 50°, and the static slip angle of the cutting edge curve is taken as 0.06.

2.6 Parametric design and analysis of front and rear knife axes

For improving the efficiency of saline soil-straw agglomerate crushing and burying, it is necessary to design and analyze the relative position structural parameters of the front and rear cutter shafts, as shown in Figure 11, which mainly include the horizontal distance between the two shafts, L_1, the ploughing depth of rotary tillage knives in the front shaft, H_1, the vertical distance, H_2, and the ploughing depth of the rotary tillage knives in the rear shaft, H_3, and so on. If L_1 is too large, the two axes will produce congestion phenomenon, if L_1 is too small, it will cause the phenomenon of straw entanglement.

In the horizontal direction, the stubble cutter shaft needs to fulfil the following conditions at the leftmost and rightmost ends.

$$\begin{cases} L_1 \ge R + R_1 + r_1 \\ L_1 - R - R_1 \le l_s \end{cases} \tag{21}$$

In the vertical direction, the stubble cutter shaft needs to fulfil the following conditions at the uppermost and lowermost ends.

$$\begin{cases} H_2 \le h_s \\ r_2 \ge R_1 - (H_2 + R - h) \end{cases} \tag{22}$$

where, l_s is the horizontal distance of the highest point of stubble

knife throwing, mm, this study took the value of 200 mm; h_s is the vertical distance of the highest point of stubble knife throwing, mm, this study took the value of 180 mm; r_1 is the safe plowing distance between stubble knife and returning knife, mm, this study took the value of 40 mm; r_2 is the returning knife radial working length, mm, this study took the value of 100 mm.

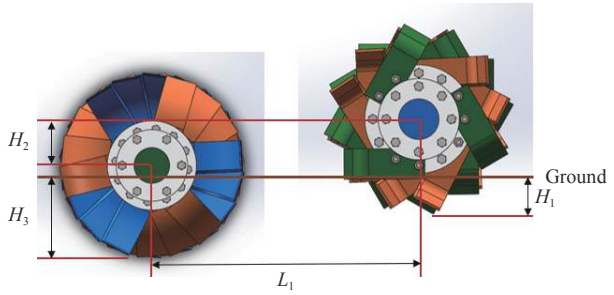

Note: L_1 is the horizontal distance between the two shafts, mm; H_1 is the ploughing depth of rotary tillage knives in the front shaft, mm; H_2 is the vertical distance between front and rear tool axis, mm; H_3 is the ploughing depth of the rotary tillage knives in the rear shaft, mm.

Figure 11 Schematic diagram of the relative positions of the double-shaft

Through the calculation, it can be obtained that the horizontal distance L_1 between the front and rear axes takes the value of 500-660 mm, and the vertical distance H_2 takes the value of 50-180 mm, and the optimal parameters are further determined through the subsequent simulation and field test.

3 Soil-straw-mechanism discrete element modeling

3.1 Soil discrete element modeling

As a further simulate the stubble rotary ploughing process in saline soil and ensure the accuracy of the discrete element simulation test, the salinity test was carried out in 0-200 mm soil depth using the dilution method according to the distribution state of the stubble root system and the requirements of peanut sowing operation. The test results showed that the salinity of 0-100 mm saline soil was 1.5‰-2.6‰, which was a low salinity soil layer, the salinity of 100-150 mm saline soil was 2.6‰-3.8‰, which was a medium salinity soil layer, and the salinity of 150-120 mm saline soil was 3.8 ‰-4.7 ‰, which was a high salinity soil layer. According to the change of salinity in different soil layers, 0-100 mm was defined as shallow soil, 100-150 mm was defined as middle soil, and 150-200 mm was defined as deep soil for the soil basic physical shape test, and the test results are listed in Table 2.

Table 2 Parameters of soil physical properties

Depth of soil/mm	Moisture content/%	Bulk density/g·cm^{-3}	Compactness/MPa
0-100	1.62	17.25	495.78
100-150	1.75	18.47	623.54
150-200	1.83	19.32	845.63
Average	1.73	18.34	654.98

Combined with the above analysis of the basic physical properties of saline soil, the layered soil discrete element modelling was carried out, the radius of the soil particles was set to 5 mm, and the following three soil types were defined by the combination of the discrete element particles: single-grained soil model, double-grained soil model, and block soil model, as shown in Figure 12. In order to simulate the state of soil fragmentation during the actual stubble removal operation, Hertz-Mindlin with Bonding is used as the soil-soil discrete element bonding model in this paper, and the ZJ-1C strain-controlled straight shear instrument as well as the three-axis compression testing machine are used, based on the test results of soil elastic modulus of 1.89 MPa and internal friction angle of 22.54°, the soil parameter calculation method of reference[30-32] was measured by approximate conversion, and the main contact parameters and physical properties of soil particles were determined after comprehensive analysis, as listed in Table 3.

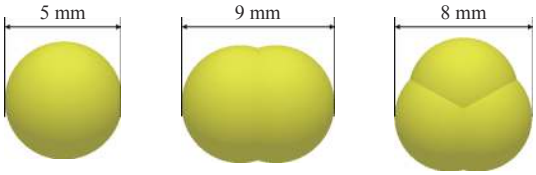

Figure 12 Soil discrete element particle modelling

Table 3 Soil discrete element model parameters

Parameter	Value
Poisson's ratio of soil	0.41
Shear modulus of soil	2.3×10^6
Coefficient of recovery of soil particles	0.59
Coefficient of static friction of soil particles	0.55
Coefficient of dynamic friction of soil particles	0.13
Soil particle bonding radius/mm	5.2
Critical tangential stress of soil particles/Pa	2.0×10^5
Critical normal stress of soil particles/Pa	3.0×10^5
Soil particle tangential bond stiffness/N·m^{-1}	3.5×10^6
Soil particle normal bond stiffness/N·m^{-1}	2.3×10^6

3.2 Straw discrete element modeling

To investigate the movement law of wheat straw during rotary ploughing and stubble removal, discrete element modelling of wheat straw with different morphologies was carried out in this paper, as shown in Figure 13. Meanwhile, in order to facilitate the analysis of the factors affecting the impact of wheat straw fragmentation, Hertz-Mindlin with Bonding was used as the straw-straw discrete element bonding model, based on the test results of the soil elastic modulus of 7.8×10^5 Pa and the angle of internal friction of 15.35°. According to the Hertz-Mindlin with Bonding particle contact model applied to the research results in the aspect of straw, refer to the literature[33-35] straw parameter calculation method approximate conversion, comprehensive analysis to determine the main contact parameters and physical properties of wheat straw particles, as listed in Table 4.

Figure 13 Discrete meta-particle modelling of wheat straw

Table 4 Straw discrete element model parameters

Parameter	Value
Density/kg·m^{-3}	235
Poisson's ratio of straw	0.39
Shear modulus of straw	1.0×10^6
Coefficient of recovery of straw	0.43
Coefficient of static friction of straw	0.11
Coefficient of dynamic friction of straw	0.05
Straw particle bonding radius/mm	3.5
Critical tangential stress of straw/Pa	6.0×10^5
Critical normal stress of straw /Pa	4.0×10^5
Straw tangential bond stiffness/N·m^{-1}	5.5×10^6
Straw normal bond stiffness/N·m^{-1}	4.3×10^6

3.3 Theoretical analysis of contact modeling

It's important to investigate the principle of soil-soil and straw-straw fragmentation under the action of stubble knife and field return knife, this study established a schematic diagram of the particle contact principle of Hertz-Mindlin with Bonding, as shown in Figure 14, a bonding region will be formed automatically between neighbouring particles, which can withstand both tangential and normal displacements, and when the particles are subjected to external impacts, there are the following mechanical relationships:

$$\begin{cases} \delta F_n = -v_n k_n A \delta_t \\ \delta F_t = -v_t k_t A \delta_t \\ \delta T_n = -w_n k_t A \delta_t \\ \delta T_t = -w_t k_t \dfrac{j}{2} \delta_t \end{cases} \tag{23}$$

$$\begin{cases} A = \pi R_a^2 \\ J = \dfrac{1}{2} \pi R_a^4 \end{cases} \tag{24}$$

where, V_n is the normal velocity, m/s; V_t is the tangential velocity, m/s; k_n is the normal stiffness, N/m; k_t is the tangential stiffness, N/m; A is the unit contact area, mm^2; J is the moment of inertia, mm^4; δ_t is the time step, s.

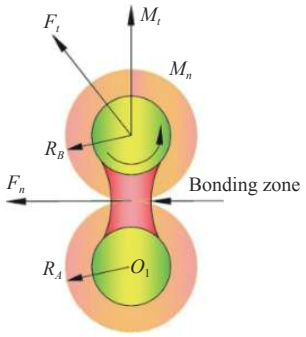

Note: O_1 and O_2 is the center of the circle of the soil model; R_A and R_B is the radius of the soil model, m; F_n is the normal contact force, N; F_t is the tangential contact force, N; M_n is the normal moment, Nm; M_t is the tangential moment, N·m.

Figure 14 Soil contact particle modelling

When the bonded region is fractured, the normal and tangential stresses between the particles reach the maximum, at which time the normal and tangential stresses are σ_{max} and τ_{max}, respectively, and the following mechanical relationship exists:

$$\begin{cases} \sigma_{max} < \dfrac{-F_n}{A} + \dfrac{2T_t}{J} R_a \\ \tau_{max} < \dfrac{-F_t}{A} + \dfrac{T_n}{J} R_a \end{cases} \tag{25}$$

where, σ_{max} is the normal stress, N; τ_{max} is the tangential stress, N; R_B is the radius of particle bonding, mm.

3.4 Soil-straw-mechanism discrete element simulation test

This paper establishes a length×width×height (1750 mm×2580 mm×1350 mm) implement-soil-straw agglomerate discrete element model as shown in Figure 15. In order to ensure the accuracy of the simulation test, the experimental simulation step size was set to 3.1×10^{-6}, the grid cell size was 6 mm, and the data collection time interval was 0.01 s[36-39]. In order to investigate the movement law of straw and soil during the test, this paper systematically investigated the soil-straw transport law of 0-100 mm shallow layer soil, 100-150 mm middle layer soil, 150-200 mm deep layer soil and straw in the vertical and horizontal directions, and set up vertical-1, vertical-2, vertical-3 in the vertical direction, and L_1, L_2, L_3 in the horizontal direction, respectively. L_1, L_2, and L_3 were set in the vertical direction and in the horizontal direction, respectively, to carry out experimental analyses. The forward speed of the whole machine was set at 1 km/s, the rotational speed of the stubble cutter shaft was 430 r/min, and the rotational speed of the field return cutter shaft was 280 r/min for simulation test.

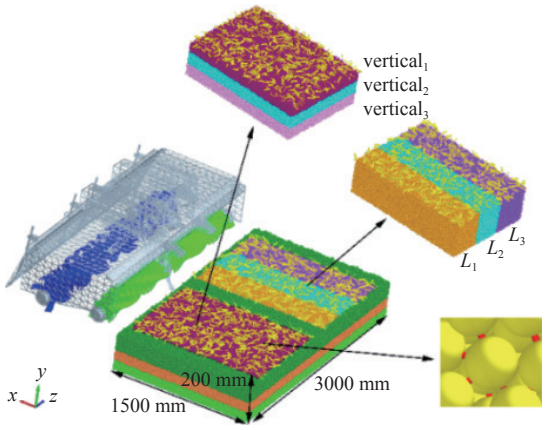

Figure 15 Soil-straw-mechanism discrete meta-modelling

Before the operation, different forms of straw were evenly spread in the vertical direction vertical$_1$, vertical$_2$, vertical$_3$, and horizontal direction L_1, L_2, L_3, and as the simulation experiment was carried out, the soil-straw agglomerates in the area A and B were crushed and buried under the action of the stubble cutter and the returning cutter as shown in Figure 16.

To systematically investigate the soil-straw transport rules under multi-temporal conditions in regions A and B, and to further analyze the factors affecting rotary plowing and stubble removal, this paper analyzed the soil-straw-gear operation process in regions A and B from a detailed point of view, as shown in Figure 17. In this study, the particle morphology is set as vector, at the moment of 1.5 s, the stubble knife disturbs the shallow soil, middle soil and deep soil from top to bottom, from near to far, and the straw-soil under the action of the stubble knife gradually generates the tendency of movement along the tangential direction of the knife tip. As the simulation test continues, the returning knife realizes the secondary crushing and deep burial of soil-straw from bottom to top, and the straw-soil is thrown along the tangential direction of the returning knife under the effect of inertia, forming a continuous particle flow of straw-plant-soil at the end of the soil-crushing cover plate, and at the same time, the soil of each layer is fully mixed after the operation.

3.5 Single-factor test analysis

Due to the high degree of soil sclerosis in saline-alkali lands, the working resistance is larger during the operation, and the forward speed is too fast resulting in the reduction of the rate of returning to the field and the rate of soil crushing, and even the phenomenon of stalling, according to the soil condition of saline-alkali lands, the operation generally adopts the low speed of the tractor in 1-3 gears, and the range of the forward speed is determined to be 1.0-5.0 km/h. Combined with the theoretical analysis of the previous article, this paper takes the forward speed, the horizontal distance L_1, and the vertical distance H_2 as the test factors, with the straw return rate and soil crushing rate as the test indicators, focusing on exploring the changes in the quality of straw

return and soil crushing by the changes in the test factors in the area A, of which the straw return rate Y_1 and soil fragmentation rate Y_2 are calculated by following equations:

$$Y_1 = \left(1 - \frac{Q_2}{Q_1}\right) \times 100\% \quad (26)$$

$$Y_2 = \left(1 - \frac{M_2}{M_1}\right) \times 100\% \quad (27)$$

where, Y_1 is the straw return rate, %; Y_2 is the soil fragmentation rate, %; Q_1 is the amount of straw before operation; Q_2 is the amount of straw after operation; M_1 is the number of soil bonding before the operation; M_2 is the number of soil bonding after the operation.

The pattern of change of different forward speeds for straw return rate and soil fragmentation rate is shown in Figure 18a, with the increase of forward speed, straw fielding rate simulation value and experimental value showed a trend of increasing and then decreasing, when the forward speed is 2 km/h, the coefficient of variation of straw fielding rate is larger, the simulation value and the experimental value are 82.53% and 75.12% respectively, when the forward speed is 3 km/h, the coefficient of variation of straw fielding rate is smallest, the simulation value and the experimental value are 90.12% and 86.58%, respectively. When the forward speed is 3 km/h, the coefficient of variation of the straw return rate is the smallest, and the simulated and experimental values are 90.12% and 86.58%, respectively. The main reason is that with the increase of the forward speed, the simulated and experimental values of the soil fragmentation rate show a decreasing trend, which affects the efficiency of the straw return to the field in deep burial. As shown in Figure 18b, when the forward speed is 1 km/h, the coefficient of variation of soil fragmentation rate simulation value is the smallest, and the test result is 93.12%, and when the forward speed is 2 km/h, the coefficient of variation of soil fragmentation rate of test value is the smallest, and the test result is 85.85%.

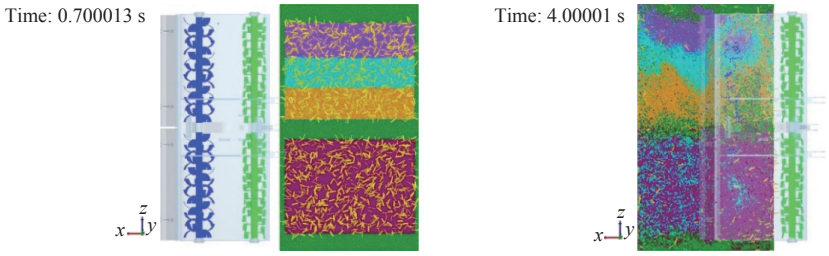

a. Before and after the simulation test b. After the simulation test

Figure 16 Amount of straw before and after the simulation test

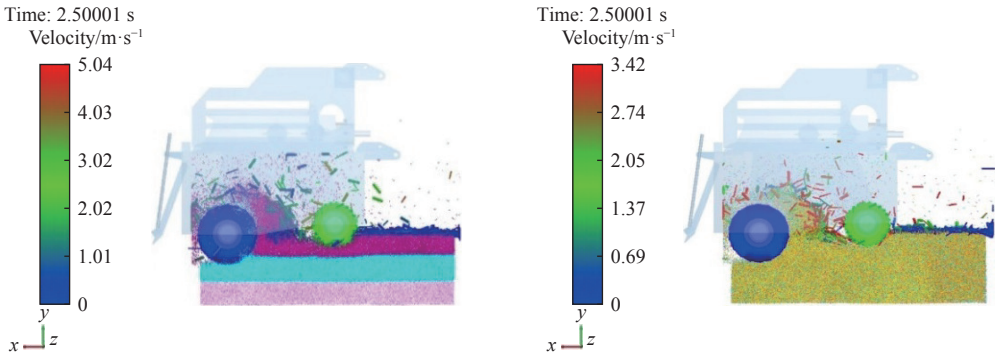

a. Region A b. Region B

Figure 17 Soil-straw movement state in region A and B at the moment of 2.5 s

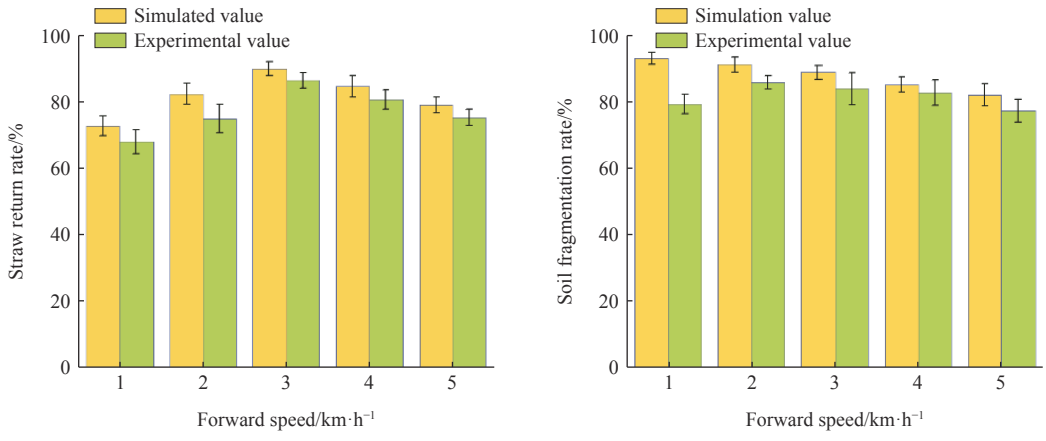

a. Rate of straw return to field b. Soil fragmentation rate

Figure 18 Effects of forward speed on the rate of straw return to field and soil fragmentation rate

The patterns of change of straw return rate and soil fragmentation rate with different horizontal spacing are shown in Figure 19. With the increase of horizontal spacing, the simulated and experimental values of straw return rate decreased gradually, and the coefficient of variation of the simulated value of straw return rate was the smallest when the horizontal spacing was 580 mm, and the simulated value was 77.85%, and the coefficient of variation of experimental value of straw return rate was the smallest when the horizontal spacing was 620 mm, and the experimental value was 72.62%. With the increase of horizontal spacing, the simulation and test values of soil fragmentation rate showed an overall trend of increasing and then decreasing, and the coefficients of variation between the simulation and test values were the smallest when the horizontal spacing was 580 mm and 620 mm, and the test results were 89.75% and 82.58%, respectively.

The patterns of change of different vertical spacing for straw return rate and soil fragmentation rate are shown in Figure 19. With the increase of vertical spacing, the simulated and experimental values of straw return rate increased gradually, and the coefficient of variation between the simulated and experimental values of straw return rate was the smallest when the vertical spacing was 115 mm and the experimental results were 91.82% and 88.58%, respectively, and the coefficient of variation was the largest when the experimental results were at 180 mm. At the same time, the straw return efficiency was the lowest. As shown in the Figure 20, with the increase of vertical spacing, the simulated and experimental values of soil fragmentation rate decreased gradually. In the interval of 50.0-147.5 mm, the simulated and experimental values of soil fragmentation rate tended to be stable, when the vertical distance was 147.5 mm, the coefficient of variation of soil fragmentation rate was the smallest, and the experimental results were 84.85% and 82.77%, respectively, and the coefficient of variation of experimental values of soil fragmentation rate was the largest and the soil fragmentation rate was the lowest when it was 180 mm.

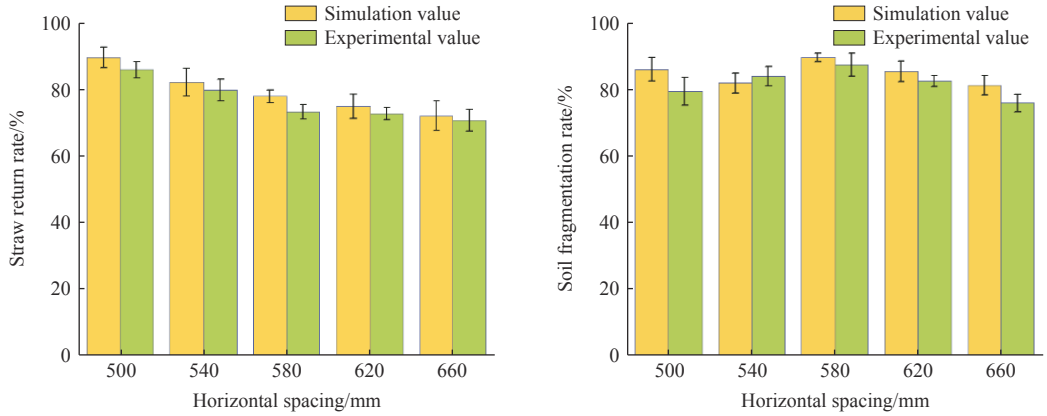

a. Rate of straw return to field b. Soil fragmentation rate

Figure 19 Effects of horizontal spacing on the rate of straw return to field and soil fragmentation rate

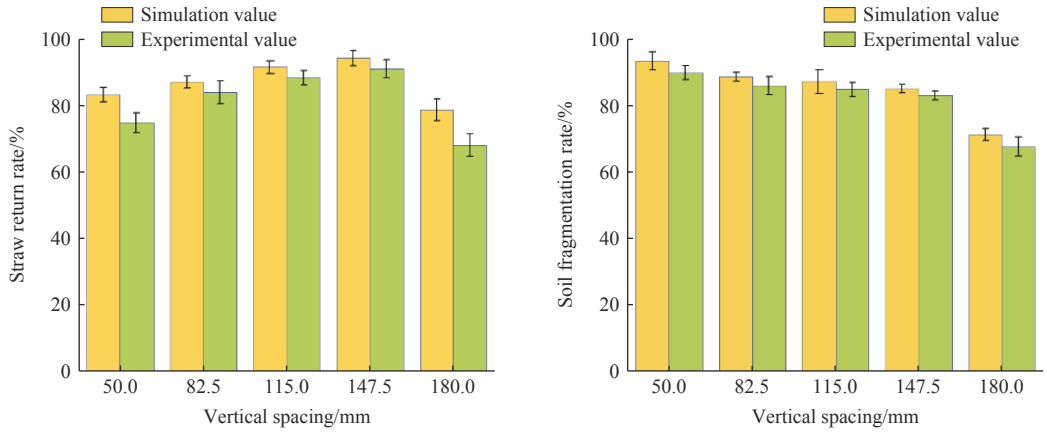

a. Rate of straw return b. Rate of soil fragmentation

Figure 20 Effects of vertical spacing on the rates of straw return and soil fragmentation

3.6 Experimental optimization and analysis

In order to explore the machine forward speed, horizontal spacing, vertical spacing for soil-straw agglomerates crushed the best combination of parameters, combined with the forward speed x_1, horizontal spacing x_2, vertical spacing x_3 test factors for the straw return rate and soil fragmentation rate of the law of change, the application of Design-Expert to establish a three-factor, three-level combination of experiments, the test code as listed in Table 5.

The results of the discrete element simulation test are listed in Table 6, and the significance analysis of variance and regression coefficients of the straw return rate Y_1 and soil fragmentation rate Y_2 was carried out in combination with Design-Expert, and the results of the analysis of variance of the straw return rate Y_1 and soil fragmentation rate Y_2 were obtained as listed in Tables 6 and 7.

The results of ANOVA of straw return rate Y_1 are shown in Table 8, in which the P value of the regression model is less than 0.01, the misfit term is 0.2418>0.05, and the coefficient of determination is 0.9894, which indicates that the regression model of straw return rate Y_1 has a good fit. From Table 7, the primary term coefficients A, B, C and the secondary term coefficients A^2, B^2

had highly significant effects on the straw return rate Y_1. The effects of each experimental factor on the significance of straw return rate were in descending order: forward speed>vertical spacing> horizontal spacing. The regression equation of straw return rate Y_1 was obtained by combining with ANOVA:

$$Y_1 = 80.27 - 6.17x_1 - 2.86x_2 + 2.50x_3 - 0.39x_x x_2 + 0.24x_1x_3 + 1.04x_2x_3 + 2.21x_1^2 - 5.86x_2^2 - 0.52x_3^2$$

Table 5 Test factor code

Code	Factor		
	forward speed x_1/km·h^{-1}	horizontal spacing x_2/mm	vertical spacing x_3/mm
–1	1.0	500	50
0	2.5	580	115
1	5.0	660	180

Table 6 Discrete element simulation test results

Serial number	Factor			Y_1/%	Y_2/%
	x_1	x_2	x_3		
1	–1	–1	0	85.24	87.24
2	1	–1	0	72.75	68.54
3	–1	1	0	81.27	78.58
4	1	1	0	67.21	69.54
5	–1	0	–1	85.54	83.52
6	1	0	–1	73.67	77.23
7	–1	0	1	89.76	92.57
8	1	0	1	78.85	81.48
9	0	–1	–1	75.61	76.47
10	0	1	–1	66.85	69.82
11	0	–1	1	78.86	82.57
12	0	1	1	74.24	77.82
13	0	0	0	81.25	84.86
14	0	0	0	79.25	82.58
15	0	0	0	79.76	81.67
16	0	0	0	80.42	82.72
17	0	0	0	80.65	82.68

Table 7 Analysis of variance for straw return rate

Source	Sum of squares	degrees of freedom	Mean square	F	p
Model	586.88	9	65.21	72.82	<0.0001
A	304.18	1	304.18	339.67	<0.0001
B	65.49	1	65.49	73.14	<0.0001
C	50.20	1	50.20	56.06	0.0001
AB	0.62	1	0.62	0.69	0.4342
AC	0.23	1	0.23	0.26	0.6276
BC	4.28	1	4.28	4.78	0.0649
A^2	20.53	1	20.53	22.93	0.0020
B^2	144.43	1	144.43	161.28	<0.0001
C^2	1.14	1	1.14	1.27	0.2973
Residual	6.27	7	0.90		
Lack of fit	3.84	3	1.28	2.11	0.2418
Pure error	2.43	4	0.61		
Sum	593.15	16			

The results of ANOVA of soil fragmentation rate Y_2 are listed in Table 8, in which the p value of the regression model is less than 0.01, the misfit term is 0.1206>0.05, and the coefficient of determination is 0.9681, which indicates that the regression model of soil fragmentation rate Y_2 has a good fit. As can be seen from the table, the primary term coefficients A, B, C and the secondary term coefficient C^2 have a highly significant effect on the soil fragmentation rate Y_2. The effects of each test factor on the significance of soil fragmentation rate were in descending order: forward speed>vertical spacing>horizontal spacing. The regression equation on soil fragmentation rate Y_2 was obtained by combining with ANOVA:

$$Y_2 = 82.90 - 5.64x_1 - 2.38x_2 + 3.42x_3 + 2.41x_x x_2 - 1.20x_1x_3 + 0.48x_2x_3 + 0.052x_1^2 - 6.98x_2^2 + 0.75x_3^2$$

Table 8 Analysis of variance for soil fragmentation

Source	Sum of squares	Degrees of freedom	Mean square	F	p
Model	629.75	9	69.97	23.570	0.0002
A	254.48	1	254.48	85.710	<0.0001
B	45.41	1	45.41	15.300	0.0058
C	93.84	1	93.84	31.610	0.0008
AB	23.33	1	23.33	7.860	0.0264
AC	5.76	1	5.76	1.940	0.2063
BC	0.90	1	0.90	0.300	0.5985
A^2	0.01	1	0.01	0.004	0.9528
B^2	205.05	1	205.05	69.070	<0.0001
C^2	2.35	1	2.35	0.790	0.4035
Residual	20.78	7	2.97		
Lack of fit	15.24	3	5.08	3.670	0.1206
Pure error	5.54	4	1.38		
Sum	650.53	16			

The surface diagram of the interaction effects of forward speed, horizontal spacing and vertical spacing is shown in Figures 21 and 22. When the horizontal spacing and vertical spacing are fixed at a certain level and the forward speed increases from 1 km/h to 5km/h, the straw return rate and soil fragmentation rate decrease gradually. When the forward speed is fixed at a certain level, the straw return rate and soil fragmentation rate show a trend of increasing and then decreasing with the increase of the horizontal and vertical spacing, combined with the discrete element simulation, the main cause of this phenomenon is that in the operation of dual-axis rotary ploughing machine, the front axle mainly crushes and throws the wheat straw, and at the same time carries out the shallow soil fragmentation, and the rear axle mainly buries the straw and at the same time carries out the deep soil burying. When the horizontal spacing is too small, it is easy to cause the soil and straw blockage, reduce the operational efficiency, when the horizontal spacing is too large, the initial speed of the soil-straw thrown by the front axle cannot be successfully transitioned to the rear axle, resulting in most of the straw thrown on the surface, resulting in the reduction of the rate of straw return to the field as well as the soil crushing rate, so when the horizontal spacing is gradually increased, the rate of straw return to the field and the rate of soil crushing with the increase in the horizontal spacing and the vertical spacing was increase and then decrease.

In this study, an objective function with forward speed, horizontal distance and vertical distance as constraints was established to improve the soil fragmentation rate and straw return rate during the test.

$$\begin{cases} \max\ Y_1 \\ \max\ Y_2 \\ \text{s.t.} \begin{cases} 1\ \text{km/h} \le x_1 \le 5\ \text{km/h} \\ 500\ \text{mm} \le x_2 \le 660\ \text{mm} \\ 50\ \text{mm} \le x_3 \le 180\ \text{mm} \end{cases} \end{cases} \quad (28)$$

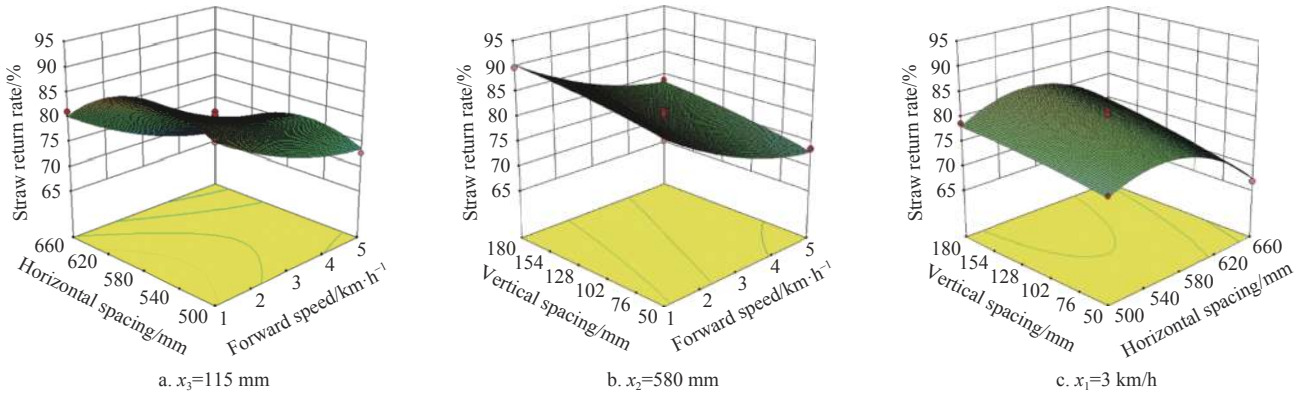

a. x_3=115 mm b. x_2=580 mm c. x_1=3 km/h

Figure 21 Straw return rates with different factors

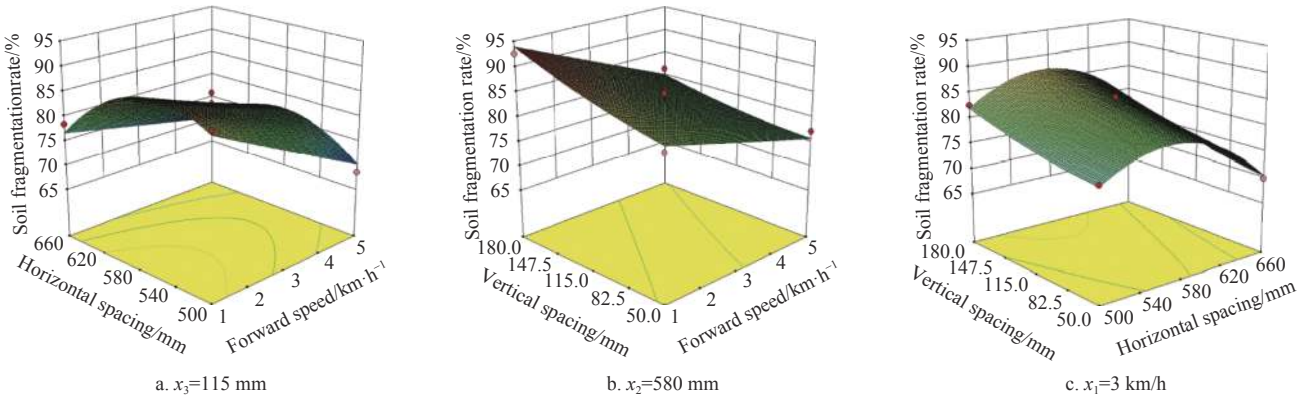

a. x_3=115 mm b. x_2=580 mm c. x_1=3 km/h

Figure 22 Soil fragmentation rates with different factors

The objective function was solved by using Design-Expert post-processing optimization, and the optimal working parameters of the double-axis layered rotary stubble machine were obtained: the forward speed was 1.07 km/h, the horizontal spacing was 569.55 mm, and the vertical spacing was 176.59 mm, and the straw returning rate was 90.07% and the soil breakage rate was 93.43%. In order to verify the accuracy of the test results, the best working parameters were imported into the discrete element model, and five repeatable tests were carried out, and the average test results were taken, at this time, the straw returning rate was 92.58%, the soil breakage rate was 91.72%, and the maximum error was 2.71%, indicating the accuracy of the experimental analysis model.

From the test results, it is clear that the discrete element simulation can effectively evaluate soil-straw-mechanism interaction mechanism. This study analyzed the straw-soil transport law under different operating parameters from the microscopic point of view by discrete element simulation, effectively predict the pattern of change between test indicators (the straw returning rate and the soil breakage rate) and test factors (forward speed and horizontal and spacing vertical spacing), and the best structural parameters were obtained by Design-Expert, further verify the correctness of the theoretical analysis.

4 Field performance test

4.1 Experimental program and conditions

In order to test the actual performance of the double-axis layered rotary stubble machine in saline-alkali land, the best working parameters were determined by combining the simulation test results and the actual processing requirements as follows: the forward speed of 1.0 km/h, the horizontal spacing of 570 mm and the vertical spacing of 171 mm, and the double-axis layered rotary stubble machine on saline land was developed. June 22, 2022 in the Yellow River Delta Agricultural High-tech Industrial Demonstration Area of the Yellow River Delta of Shandong Province. The soil water content was 12%-16%, the soil firmness was 500-1000 kPa within 0-200 mm, the soil salinity ranged from 2.5‰-4.2‰, the stubble height of wheat straw was 10-15 cm, the supporting equipment was Deutz-Fahr 1804 tractor.

4.2 Test method

The machine's forward speed was 1 km/h, working depth of the machine was 160 mm, the rotational speed of the cutter shaft of the front axle was 430 r/min, the rotational speed of the cutter shaft of the rear axle was 280 r/min. and it was paired with peanut joint planter to evaluate the operational effect.

The straw return rate is tested by measuring the mass of all straw m_1 in the 1 m×1 m area in the unoperated plots, and measuring the mass of the remaining straw m_2 in the area again after the operation, then the straw return rate is calculated as,

$$Y_1 = \left(1 - \frac{m_2}{m_1}\right) \times 100\% \tag{29}$$

where, m_1 is the total mass of straw before operation in the experimental area, g; m_2 is the total mass of straw after operation in the experimental area, g.

According to (GB/T 5668-2017) on the measurement of soil fragmentation rate, the 0.5 m×0.5 m test area was randomly measured in the area after rotary ploughing and stubble removal, and the soil blocks in the area were divided into three grades of less than 4 cm, 4-8 cm and more than 8 cm according to their longest sides, and the soil fragmentation rate was taken as the percentage of the mass of soil blocks with sides less than 4 cm in the whole plough layer, in order to ensure test precision, 10 measurement areas were measured randomly, and its calculation method was:

$$Y_2 = \frac{m_a - m_3}{m_a} \times 100\% \tag{30}$$

where, m_a is the total mass of soil blocks in the full tillage layer of the test area, g; m_3 is the mass of soil blocks with the longest side greater than 4 cm in the test area, g.

Ten groups of 1.5 m×1.5 m test areas were randomly selected in the operation area for ploughing depth testing and the test results were averaged and calculated as follows:

$$Y_3 = \left(1 - \frac{\sqrt{\sum_{i=1}^{n}(a_i - a)^2 / n}}{\sum_{i=1}^{n} a_i / n}\right) \times 100\% \quad (31)$$

where, Y_3 is the depth of tillage stability, %; n is the number of measurement points in the same test area; a is the average depth of tillage, mm; a_i is the depth of plowing at point i, mm.

4.3 Analysis of the test results

Double-axis stratified rotary ploughing stubble machine with peanut starting joint planter joint operation, the operation results are shown in Figure 23. According to (NT/Y 499-2013 Standard of Practice for Rotary Tillers), 5 groups of measurement points were randomly selected to take the average value as the test results, and the test results are listed in Table 9.

Figure 23 Wheat straw return trial

Table 9 Field test results

Test serial number	Straw return rate/%	Soil fragmentation rate/%	Depth of tillage stability/%
1	91.25	91.52	91.46
2	91.68	92.25	90.85
3	92.14	92.12	91.52
4	91.12	91.75	92.12
5	91.75	91.89	91.65
Maximum value	92.14	92.25	92.12
Minimum value	91.12	91.52	90.85
Average value	91.59	91.90	91.52
Standard deviation	0.41	0.29	0.46

According to (NT/Y 499-2013 standard of practice for rotary tillers), the straw return rate should be more than 80%, the soil fragmentation rate should be more than 80%, the depth of tillage stability should be more than 85%, It can be seen from Table 9, the straw return rate was (91.59±0.41)%, the soil fragmentation rate was(91.90±0.29)%, the depth of tillage stability was (91.52±0.46)%, which met the requirements for peanut seed bed preparation in saline-alkali land.

5 Conclusions

This study proposed a dual-axis stratified rotary stubble cutter with front-axis positive rotation and rear-axis counter-rotation for peanut seed bed preparation in saline-alkali land, which comprehensively covers the study of rotary tillage knife-straw interaction mechanism, the kinetic analysis of straw cutting process, the rotary tillage knife-straw-soil discrete element simulation test, and the design of the structural parameters of the double cutter shaft. The machine can be used for the preparation of seed beds for saline soils with different straw contents.

By conducting a kinetic analysis of straw-soil-rotary blade under the action of positive and negative rotation, and the structural and operational parameters of the front and rear axes of the rotary tillage knives were determined. Meanwhile, a discrete element simulation test was carried out with forward speed, horizontal spacing and vertical spacing as the test factors, and straw return rate and soil fragmentation rate as the test indexes to investigate the dynamic process of straw-soil agglomerate fragmentation from the microscopic. According to the optimization analysis of the Design-Expert test, the best working parameters were: forward speed 1.07 km/h, horizontal spacing 569.55 mm, vertical spacing 176.59 mm, at which time the straw return rate was 90.07%, and the soil fragmentation rate was 93.43%. In order to verify the performance of double-axis stratified rotary tiller in saline-alkali land, the field tests was conducted with straw return rate, soil fragmentation rate and the depth of tillage stability as the test indexes, and the results showed that: the straw return rate was (91.59±0.41)%, the soil fragmentation rate was (91.90±0.29)%, the depth of tillage stability was (91.52±0.46)%, which met the requirements for peanut seed bed preparation in saline-alkali land.

Acknowledgements

The authors acknowledge that this work was financially sponsored by the Shandong Province Key R&D Program (Major Science and Technology Innovation Project) (Grant No. 2021CXGC010813) and Saline land tillage mechanization equipment research and development, manufacturing and popularization of application (Grant No. NJYTHSD-202314).

[References]

[1] Xiao W Z, Kong D P, Duan J, Wang X M, Wang J T, Wang D S. Design and test of peanut no-tillage planter under the coverage of the wheat straw. Journal of Agricultural Mechanization Research, 2022; 44(7): 128–132. (in Chinese)

[2] Liao Q X, Wu H M, Zhang Q S, Zhang J Q, Ao Q, Wang L. Design and experiment of driven disc plow and double-edged rotary tillage combined tiller. Transactions of the CSAM, 2023; 54(7): 99–110, 195. (in Chinese)

[3] Yang Y S, Wu F, Zhao Y P, Hu Z C, Gu W F, Ding Q S. The study of the effect of tillage components on the quality of strip rotary ploughing cultivation. Journal of Chinese Agricultural Mechanzation, 2022; 43(12): 184–189. (in Chinese)

[4] Zhang C Y, Kang J M, Zhang N N, Li W H, Jian S C. Peanut planting mechanization key technology research status and development analysis. Transactions of the Agricultural Equipment and Vehicle Engineering, 2019; 57(S1): 27–34.

[5] Zhao H B, Huang Y X, Liu Z D, Liu W Z, Zheng Z Q. Applications of discrete element method in the research of agricultural machinery: A review. Agriculture, 2021; 11: 425.

[6] Wang L J, Zhou B, Wan C, Zhou L. Structural parameter optimization of a furrow opener based on EDEM software. Int J Agric & Biol Eng, 2024; 17(3): 115–120.

[7] Zhang X Y, Hu X, Zhang L X, Kheiry A N O. Simulation and structural parameter optimization of rotary blade cutting soil based on SPH method. Int J Agric & Biol Eng, 2024; 17(3): 82–90.

[8] Du J, Heng Y F, Zheng K, Luo C M, Zhu Y M, Zhang J M, et al. Investigation of the burial and mixing performance of a rotary tiller using discrete element method. Soil Tillage Res, 2022; 220: 105349.

[9] Mohammadi F, Maleki M R, Khodaei J. Control of variable rate system of

a rotary tiller based on real-time measurement of soil surface roughness. Soil Tillage Res, 2022; 215: 105216

[10] Yu J Q, Fu H, Li H, Shen Y F. Application of discrete element method to research and design of working parts of agricultural machines. Transactions of the CSAE, 2005; 21(5): 1–6. (in Chinese)

[11] Xu Y, Li H Y, Huang W B. Modeling and methodological strategy of discrete element method simulation for tillage soil dynamics. Transactions of the CSAE, 2003; 19(2): 34–38. (in Chinese)

[12] Zeng Z W, Ma X, Cao X L, Li Z H, Wang X C. Critical review of applications of discrete element method in agricultural engineering. Transactions of the CSAM, 2021; 52(4): 1–20. (in Chinese)

[13] Li M L, Liao Q X, Pei L M, Liao Y T, Wang L, Zhang Q S. Design and experiment of rotary-cut micro-ridge seedbed device for rapeseed direct seeding machine. Transactions of the CSAM, 2023; 54(5): 47–58, 90. (in Chinese)

[14] Chen G B, Wang Q J, Li H W, He J, Wang X H, Zhang X Y, et al. Experimental research on vertical straw cleaning and soil tillage device based on Soil-Straw composite model. Computers and Electronics in Agriculture, 2024; 216: 108510.

[15] Zhou H, Zhang C L, Zhang W L, Yang Q J, Li D, Liu Z Y, et al. Evaluation of straw spatial distribution after straw incorporation into soil for different tillage tools. Soil Tillage Res, 2020; 196: 104440.

[16] Jia H L, Wang L C, Li C S, Tan H J, Ma C L. Combined stalk–stubble breaking and mulching machine, Soil Tillage Res. 2010; 107(1): 42–48.

[17] Torotwa I, Ding Q S, Makange N R, Liang L, He R Y. Performance evaluation of a biomimetically designed disc for dense-straw mulched conservation tillage, Soil Tillage Res, 2021; 212: 105068.

[18] Barbosa L A P. Modelling the aggregate structure of a bulk soil to quantify fragmentation properties and energy demand of soil tillage tools in the formation of seedbeds, Biosystems Engineering, 2020; 197: 203–215.

[19] Saunders C, Ucgul M, Godwin R J. Discrete element method (DEM) simulation to improve performance of a mouldboard skimmer. Soil Tillage Res., 2021; 205: 104764.

[20] Azimi-Nejadian H, Karparvarfard S H, Naderi-Boldaji M. Weed seed burial as affected by mouldboard design parameters, ploughing depth and speed: DEM simulations and experimental validation. Biosystems Engineering, 2022; 216: 79–92.

[21] Shaikh S A, Li Y M, Ma Z, Chandio F A, Tunio M H, Liang Z W, et al. Discrete element method (DEM) simulation of single grouser shoe-soil interaction at varied moisture contents. Computers and Electronics in Agriculture, 2021; 191: 106538.

[22] Lu Q, Liu F J, Liu L J, Liu Z J, Liu Y Q. Establishment and verification of discrete element model for seed furrow soil-seed-covering device. Transactions of the CSAM, 2023; 54(10): 46–57. (in Chinese)

[23] Zhang C, Fan X H, Li M S, Li G, Zhao C K, Sun W L. Simulation analysis and experiment of soil disturbance by chisel plow based on EDEM. Transactions of the CSAM, 2022; 53(S2): 52–59. (in Chinese)

[24] Zhu Y H. Research on the working mechanism and consumption reduction of rotary burial blade roller for straw returning. Hubei: Huazhong Agricultural University, 2019. (in Chinese)

[25] Wang J F, Yang D Z, Wang Z T, Fu Z D, Wang J W, Weng W X. Design and test of rice straw double-axis deep field return machine. Transactions of the CSAM, 2023; 54(4): 21–30. (in Chinese)

[26] Pan H R, Hu J P, Luo J M, Liu W, Zhao J. Design of automatic hard-twig graft device with different diameter ratios. Journal of Agricultural Mechanization Research, 2021; 43(6): 58–65. (in Chinese)

[27] He X N, Zhang X J, Zhao Z, Shang S Q, Wang D W, Yang S. Design and optimization tests of reverse spin-throwing cyperus edulis starting device. Transactions of the CSAM, 2022; 53(5): 34–43. (in Chinese)

[28] Wang J F, Chen B W, Jiang Y, Zhu M, Xia J F, Wang J W. Design and experiment on machine for rice straw full quantity deep buried into field. Transactions of the CSAM, 2020; 51(1): 84–93. (in Chinese)

[29] Zhang X. Optimized design and experimental study of rice straw counter-rotating deep-embedded planting device. Master dissertation. Harbin: Northeast Agricultural University, 2022; 74p. (in Chinese)

[30] Zhu Y H, Xia J F, Zeng R, Zheng K, Du J, Liu Z Y. Prediction model of rotary tillage power consumption in paddy stubble field based on discrete element method. Transactions of the CSAM, 2020; 51(10): 42–50. (in Chinese)

[31] Adajar J B, Alfaro M, Chen Y, Zeng Z W. Calibration of discrete element parameters of crop residues and their interfaces with soil. Computers and Electronics in Agriculture, 2021; 188: 106349.

[32] Liu K H, Sozzi M, Gasparini F, Marinello F, Sartori L. Combining simulations and field experiments: Effects of subsoiling angle and tillage depth on soil structure and energy requirements. Computers and Electronics in Agriculture, 2023; 214: 108323.

[33] Fang H M, Ji C Y, Tagar A A, Zhang Q Y, Guo J. Simulation analysis of straw displacement in straw-soil-rotary cutter system. Transactions of the CSAM, 2016; 47(1): 60–67. (in Chinese)

[34] Guo J, Ji C Y, Fang H M, Zhang Q Y, Hua F L, Zhang C. Experimental analysis on the displacement of soil and straw after rotary tillage by forward and reverse rotation. Transactions of the CSAM, 2016; 47(5): 21–26. (in Chinese)

[35] Guan C S, Fu J J, Xu L, Jiang Z C, Wang S L, Cui Z C. Study on the reduction of soil adhesion and tillage force of bionic cutter teeth in secondary soil crushing. Biosyst. Eng, 2022; 213: 133–147.

[36] He R Y, Duan Q F, Cheng X X, Xu G M, Ding Q S. DEM Analysis of spatial distribution quality of rotary tillage straw returning. Transactions of the CSAM, 2022; 53(6): 44–53. (in Chinese)

[37] Zheng K, He J, Li H W, Zhao H B, Hu H N, Liu W Z. Design and experiment of a combined tillage machine with reverse rotation and subsoiling. Transactions of the CSAM, 2017; 48(8): 61–71. (in Chinese)

[38] Ucgul M, Fielke J M, Saunders C. 3D DEM tillage simulation: Validation of a hysteretic spring (plastic) contact model for a sweep tool operating in a cohesionless soil. Soil & Tillage and Research, 2014; 144(1): 220–227.

[39] Bechert D W, Bruse M, Hage W, Van D E R, Hoeven J G T, Hopp G. Experiments on drag-reducing surfaces and their optimization with an adjustable geometry. Journal of Fluid Mechanics. 1997; 338: 59–87.